JACS
JOURNAL OF THE AMERICAN CHEMICAL SOCIETY
pubs.acs.org/JACS
Article

Atomistic Explanation of the Dramatically Improved Oxygen Reduction Reaction of Jagged Platinum Nanowires, 50 Times Better than Pt

Yalu Chen, Tao Cheng, and William A. Goddard III*

Cite This: J. Am. Chem. Soc. 2020, 142, 8625−8632
Read Online
ACCESS | Metrics & More | Article Recommendations | Supporting Information

ABSTRACT: Pt is the best catalyst for the oxygen reduction reactions (ORRs), but it is far too slow. Huang and co-workers showed that dealloying 5 nm Ni_7Pt_3 nanowires (NW) led to 2 nm pure Pt jagged NW (J-PtNW) with ORRs 50 times faster than Pt/C. They suggested that the undercoordinated surface Pt atoms, mechanical strain, and high electrochemically active surface area (ECSA) are the main contributors. We report here multiscale atomic simulations that further explain this remarkably accelerated ORR activity from an atomistic perspective. We used the ReaxFF reactive force field to convert the 5 nm Ni_7Pt_3 NW to the jagged 2 nm NW. We applied quantum mechanics to find that 14.4% of the surface sites are barrierless for $O_{ads} + H_2O_{ads} \rightarrow 2OH_{ads}$, the rate-determining step (RDS). The reason is that the concave nature of many surface sites pushes the OH bond of the H_2O_{ads} close to the O_{ads}, leading to a dramatically reduced barrier. We used this observation to predict the performance improvement of the J-PtNW relative to Pt (111). Assuming every surface site reacts independently with this predicted rate leads to a 212-fold enhancement at 298.15 K, compared to 50 times experimentally. The atomic structures of the active sites provide insights for designing high-performance electrocatalysts for ORR.

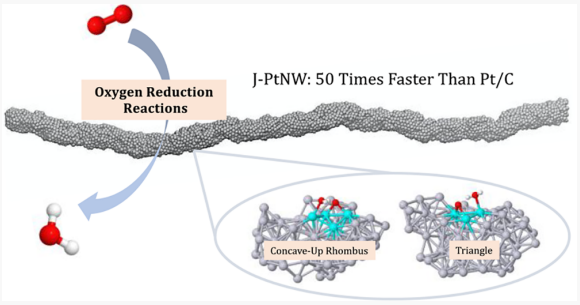

1. INTRODUCTION

Proton exchange membrane fuel cells (PEMFCs) provide the most promising means for addressing the global renewable energy supply and clean environment.[1−3] Currently, the main impediment for large-scale PEMFCs commercialization is the sluggish oxygen reduction reaction (ORR), which dramatically increases catalyst costs. Extensive efforts are underway to develop electrocatalysts for ORRs with much higher performance and lower cost.[4−6] Pt−alloy nanomaterials show enhanced performance,[7−12] especially PtNi alloys.[13−17] In particular, very dramatically improved performance has been observed in dealloyed Pt nanomaterials.[18−22] Thus, Debe and co-workers showed that Ni_7Pt_3 nanoparticles (NP) led to significantly improved ORR activity, 4 times higher than that of pure Pt and 60% higher than that for the NSTF standard $Pt_{68}Co_{29}Mn_3$ alloy.[23−26] However, no Ni was observed in the XPS, suggesting the NP was a dealloyed Pt NP. Fortunelli and Goddard (FG) used the ReaxFF reactive force field[27] to predict the structure of the dealloyed Debe NP and found that starting with 70% Ni led to a porous Pt with significant interior area exposed to the surface. FG found that the O_{ads} hydration reaction

$$O_{ads} + H_2O_{ads} \rightarrow 2OH_{ads} \quad (1)$$

is the rate-determining step (RDS) on Pt (111) and is dramatically accelerated on this porous NP compared to Pt (111).[28]

Later, Huang, Duan, Goddard, and co-workers[29] showed that dealloying 5 nm Ni_7Pt_3 nanowires (NW) led to 2 nm Pt jagged NW (J-PtNW) with 50 times faster ORR than current state-of-the-art Pt/C, but they found that all Ni was extracted! Building this dramatically improved performance into commercial fuel cells would be a game changer, dramatically decreasing the costs of hydrogen fuel cells needed to extract the power from fuel generated and stored at solar power plants to provide practical transportation without CO_2 emissions.

Although several factors, such as undercoordinated surface Pt atoms, mechanical strain, and high electrochemically active surface area (ECSA), have been suggested to contribute to this remarkably accelerated ORR activity,[29] there was no atomistic explanation about which sites on this very complex surface are

Received: December 8, 2019
Published: April 22, 2020

https://dx.doi.org/10.1021/jacs.9b13218
J. Am. Chem. Soc. 2020, 142, 8625−8632

responsible, leaving no roadmap to build this activity into practical electrodes.

To address this conundrum, we report here multiscale simulations to explain the dramatically improved performance and to characterize the atomic features of active sites responsible. Starting with the J-PtNW synthesized computationally using the ReaxFF reactive force field, we selected randomly 500 of the more than 10 000 surface sites and carried out quantum mechanics (QM) calculations on clusters within 8 Å of the surface site. Here, we considered reaction 1, the RDS on Pt (111). We observed a strong correlation between the OO distance (the distance between O_{ads} and the O of H_2O_{ads}) and the free energy barrier for reaction 1. Indeed, 14.4% of the 500 surface sites sampled are barrierless of reaction 1 at room temperature compared to 0.29 eV for Pt (111) and hence increased reaction rate. We then modeled the reaction rates of all surface sites based on their OO distances and estimated the performance of the whole J-PtNW.

We found two distinct geometric patterns: triangles where the H_2O binds to one vertex and O to the other two and concave-up rhombi where O binds to one edge and the H_2O to one of the remaining two vertices.

The atomic structure of these active sites provides insights on designing high-performance electrocatalysts for ORR.

2. RESULTS AND DISCUSSION

2.1. Structure Analysis and Surface Extraction of J-PtNW. Starting with the J-PtNW synthesized using ReaxFF reactive molecular dynamics (RMD) as in the previous work,[29] we identified all surface atoms using the surface vector-based methodology. The detailed description of structure synthesis and the surface vector-based methodology are listed in S1 and S2 of the Supporting Information. The nanowire has 6926 Pt atoms, with 3881 on the surface (surface ratio 56.0%). We partitioned these surface sites into coordination groups based on the number of first-neighbor atoms using a first-neighbor cutoff at 3.50 Å based on the radial distribution functions in Figure S2a of the Supporting Information. The J-PtNW showed broader peaks with the first peak located close to the first peak of the Pt single crystal, as expected. We observed many undercoordinated and overcoordinated sites both on the surface and in the bulk. The surface site distribution versus coordination is shown in Figure S2b of the Supporting Information. For better visualization, we plotted the surface in Figure S3 of the Supporting Information with all surface sites colored by their coordination (ranging from 3 to 12). This structural analysis showed that the J-PtNW have an extremely disordered and irregular surface, making it challenging to characterize experimentally and computationally.

2.2. Bridge Nanocluster Model. To study the relationship between the structure and the catalytic activity, we need to define a physical descriptor that might correlate with the performance (reaction rate). On the basis of the reaction mechanism revealed by earlier work,[30−32] we focused on the O_{ads} hydration, reaction 1.

Our full solvent QM Metadynamics showed that this step is the rate-determining step (RDS) for applied potentials of $U \leq 0.9$ V, reversible hydrogen electrode (RHE).[30,33,34] Since this reaction requires two sites for water adsorption and oxygen adsorption, instead of the single-site nanocluster model used in our previous machine-learning studies for Copper[35,36] and Gold,[37,38] we developed a new bridge nanocluster model in this work. As shown in Figure 1, we generated the bridge nanocluster by cutting two spheres of size R around the Pt atom for water adsorption (Pt-1) and the Pt atom for oxygen adsorption (Pt-2). Then we merged these two spheres to a single nanocluster. The choice of R was based on the benchmark calculations in S3 of the Supporting Information. We found that 8.0 Å is already sufficient to provide 0.02 eV accuracy in the adsorption energy for both reactants and products. Therefore, we consider that 8.0 Å provides the best balance between accuracy and efficiency and used this cutoff throughout this work.

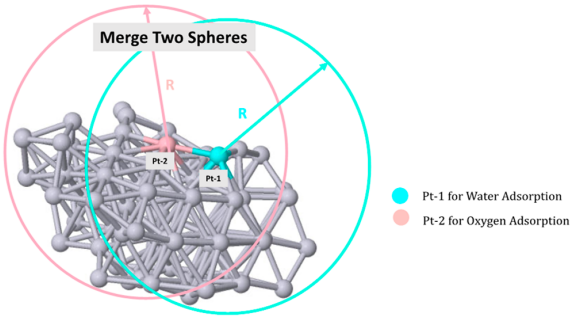

Figure 1. Bridge nanocluster model. We first cut two spheres of size R around Pt-1 (cyan atom) and Pt-2 (pink tom), where Pt-1 is specifically for water adsorption and Pt-2 is for oxygen adsorption. These two spheres are then merged to a single nanocluster. R here is optimized to 8 Å. This bridge nanocluster will later be used for DFT calculations.

2.3. OO Distance as a Physical Descriptor. We carried out DFT calculations[39] for the O_{ads} hydration, reaction 1, using the bridge nanocluster model defined in section 2.2. We chose the free energy barrier (G_a) of reaction 1 as the physical descriptor to evaluate the performance of each bridge nanocluster. We expect that sites with lower G_a should have better ORR performance. With such a disordered and irregular surface, we might have to sample all bridging surface sites to be sure to properly represent the activity of the full NW. DFT calculations on the transition state reaction barrier for the whole J-PtNW would require far too much computational resources.[40] Instead, we defined a physical descriptor, OO distance (d-OO), the distance between the O of H_2O_{ads} and the O_{ads}. Then we showed that d-OO is highly correlated with the free energy barrier (G_a), $G_a = G_{TS} - G_{Reactants}$, but much faster to calculate.

To obtain d-OO, we need only to optimize the structure of the reactants, H_2O and O. We show in Figure S7 of the Supporting Information three examples illustrating the correlation between d-OO and G_a at room temperature. By comparing to our reference case Pt(111), which has $G_a = 0.29$ eV and d-OO = 3.36 Å, we observed that shorter d-OO leads to much lower G_a (d-OO at 2.60 Å leads to $G_a = 0.00$ eV) and larger d-OO leads to higher G_a (d-OO at 3.98 Å leads to $G_a = 0.35$ eV). In addition, the thermodynamic reaction energy ($\Delta G = G_{TS} - G_{Reactants}$) does not correlate with G_a, as expected. Therefore, we used d-OO as the physical descriptor to evaluate the performance of each bridge nanocluster. All of our calculations include solvation effect using the VASPsol implicit solvation model.[41] As shown in Figures S5 and S6 in the Supporting Information, solvation affects d-OO in a non-negligible manner. The free energy barriers (G_a) at room temperature (298.15 K) are obtained by adding to the DFT

https://dx.doi.org/10.1021/jacs.9b13218
J. Am. Chem. Soc. 2020, 142, 8625−8632

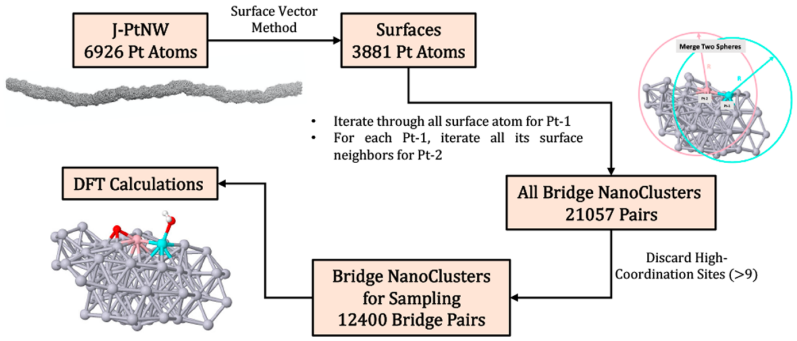

Figure 2. Generating all bridge pairs for data sampling. Starting from the J-PtNW with 6926 Pt atoms, we identified 3881 surface atoms using the surface vector methodology. Then we iterated first over the whole surface for Pt-1, and for each Pt-1 we iterated over its surface neighbors for Pt-2. In this way, we generated a total number of 21 057 bridge pairs. We showed that sites with coordination larger than 9 cannot adsorb water. Discarding these bridge pairs with coordination of Pt-1 larger than 9 leaves 12 400 bridge pairs for data sampling.

electronic energy (E), the zero-point energy (ZPE), and the enthalpy and entropy contribution from vibrational modes of surface species. More computational details of d-OO and G_a are listed in S4 and S5 of the Supporting Information.

2.4. Data Sampling for DFT Calculations (d-OO). To generate all possible bridge pairs from 3881 surface Pt atoms of the J-PtNW, we first examined Pt-1 for water adsorption of all surface Pt atoms. Then for each Pt-1 we examined its first neighbors on the surface to select Pt-2 for binding an O atom. This defines a bridge pair. The definitions of Pt-1 and Pt-2 are the same as in Figure 1. Then we cut the corresponding bridge nanoclusters from the NW. This generates the same nanocluster twice with Pt-1 and Pt-2 swapping the labels, but we consider them as different structures since Pt-1 is specifically for water adsorption and Pt-2 is specifically for oxygen adsorption. The two Pts are not identical when binding adsorbates. An example of two nanoclusters of the same coordinates but defined as different structures is shown in Figure S8 of the Supporting Information.

In this way, we generated 21 057 bridge pairs. Since H_2O binds weakly to high-coordination sites, we expect that they would be inactive for ORR. To test this, we selected randomly 50 sites for which Pt-1 has a coordination larger than 9 and calculated water adsorption. We found water desorbed from all 50 sites. Therefore, we discarded the high-coordination bridge pairs (coordination of Pt-1 > 9), which leaves 12 400 bridge nanoclusters for further sampling. This procedure is illustrated schematically in Figure 2.

We then randomly sampled 500 bridge nanoclusters from these 12 400 pairs for DFT calculations. For each nanocluster, we put water on Pt-1 and oxygen on Pt-2 and then optimized the structure to find the best conformation for the adsorbates. Solvation effects are included here using the VASPsol implicit solvation model. Additional DFT calculation details including all benchmark calculations are listed in section S4, Tables S1–S3, and Figures S5 and S6 of the Supporting Information. The sampled bridge centers are plotted back on the NW in Figure S9 of the Supporting Information. The bridge centers are distributed throughout the whole nanowire, indicating our sample is a good representation of the whole J-PtNW.

The distribution of d-OO among 500 nanoclusters is shown in Figure 3. We see that d-OO ranges from 2.50 to 6.01 Å. However, 35.2% of the sites have a d-OO distance shorter than the d-OO (3.36 Å) for Pt (111). We expect these sites to have much lower free energy barriers for O_{ads} hydration and hence

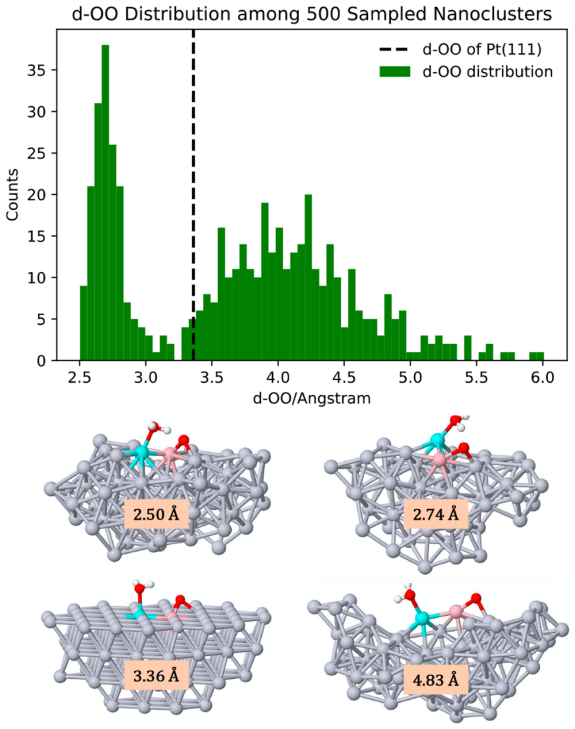

Figure 3. d-OO distribution among 500 sampled bridge nanoclusters. Our sample showed a broad range of d-OO, from 2.50 to 6.01 Å. d-OO of Pt (111) is marked in the plot as the dashed line. We observed 35.2% of the sites lying to the left to Pt (111), showing much shorter d-OO. We expect these sites to have a much lower energy barrier for O_{ads} hydration, thus leading to higher ORR performance. Four representative structures with different d-OO are attached here for understanding the correlation between structure and catalytic activities.

to contribute significantly to the dramatically improved performance of J-PtNW at ORR. To help provide a better understanding of how the geometry of different sites affects d-OO and the free energy barrier, several representative structures with different d-OO are also shown at the bottom of Figure 3.

https://dx.doi.org/10.1021/jacs.9b13218
J. Am. Chem. Soc. 2020, 142, 8625–8632

2.5. Correlation of *d*-OO with Catalytic Activity. To further understand the correlation between *d*-OO and the catalytic activity of each bridge site, we selected 18 structures with various *d*-OO and calculated the transition state and free energy barriers. The structures were selected randomly and independently but in such a way to ensure that we covered a broad range of *d*-OO. For each structure, we carried out the transition state search using the climbing image nudged elastic band (NEB) method with implicit solvation using the VASPsol tool. The free energy barriers (G_a) for the O_{ads} hydration at room temperature (298.15 K) are then obtained by adding to the DFT electronic energy (E), the zero-point energy (ZPE), and enthalpy and entropy contributions from the vibrational modes of surface species. The data for the 18 structures, including *d*-OO and free energy barriers (G_a), at room temperature are listed in Table 1. More computation details toward the transition state search are included in S5 of the Supporting Information.

Table 1. Correlation between *d*-OO and the Free Energy Barrier (G_a) at Room temperature 298.15 K

d-OO (Å)	G_a (298.15 K,eV)	*d*-OO (Å)	G_a (298.15 K,eV)	*d*-OO (Å)	G_a (298.15 K,eV)
2.50	0.00	2.76	0.01	3.50	0.20
2.56	0.00	2.80	0.06	3.57	0.19
2.60	0.00	2.93	0.12	3.70	0.14
2.64	0.00	2.99	0.10	3.75	0.40
2.68	0.00	3.12	0.16	3.98	0.35
2.74	0.01	3.36	0.29	4.22	0.28

We observed a strong correlation between *d*-OO and G_a, as shown in Table 1. The sites with small *d*-OO show low free energy barriers, especially with *d*-OO $\leq$ 2.68 Å; the O_{ads} hydration step becomes barrierless. Also, with larger *d*-OO, G_a generally becomes higher but in a nonlinear manner. Pt(111) shows *d*-OO at 3.36 Å and G_a at 0.29 eV, as given in Table 1. To better correlate *d*-OO with the catalytic activity, we used transition state theory (TST) to estimate the reaction rate as $k = (k_BT/h)\exp(-G_a/k_BT)$. The reaction rates are plotted versus *d*-OO of 18 structures in Figure 4. Here, we used the sigmoid function to fit the k(*d*-OO) curve at room temperature. The fitted curve is also shown in Figure 4 with R^2 at 0.9894.

Therefore, we found that a large portion of sites on the J-PtNW surface exhibits dramatically improved performance toward O_{ads} hydration, the RDS. We claim that this is the main contributor to the dramatically improved ORR performance. In addition, we showed that *d*-OO is a good descriptor for evaluating the catalytic activity of any specific bridge pair. The Appendix of the Supporting Information provides coordinates of the pathway for three representative structures from Table 1.

2.6. Performance Prediction of the Whole J-PtNW. Since our data set is sampled randomly and independently, we consider it to be representative of the whole J-PtNW surface. Thus, we estimated the performance of the whole nanowire by mapping the statistics of our sample back to the full NW. The J-PtNW has 6926 Pt atoms with 3881 surface atoms, which leads to 21 057 bridge pairs. Among these 21 057 pairs, 8657 are high-coordination involved pairs, which we assume are inactive. The remaining 12 400 pairs should have a similar *d*-OO distribution as the 500 samples.

To estimate the performance improvement at different temperatures, we first calculated the free energy barriers at different temperature and refit the sigmoid functions. In other words, k(*d*-OO) is dependent on T. Three examples of fitting k(*d*-OO) at different temperatures are shown in Figure S10 of the Supporting Information.

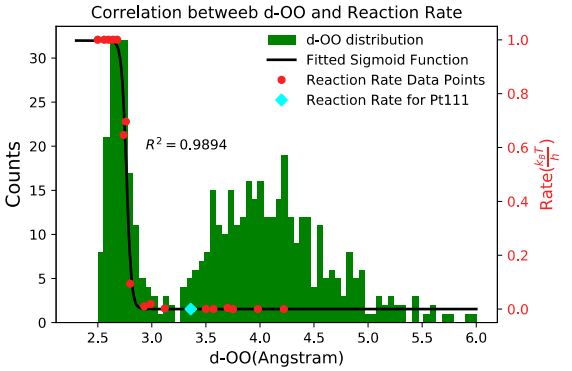

Figure 4. Correlation between *d*-OO and reaction rate. We used transition state theory (TST) to estimate the reaction rate as $k = (k_BT/h)\exp(-G_a/k_BT)$ of 18 selected structures listed in Table 1. Reaction rates are plotted in units of (k_BT/h) versus *d*-OO. We then used the sigmoid function to fit the k(*d*-OO) curve at room temperature, $k = L/(1 + \exp(A \times (d\text{-OO} - x_0))) + b$. Parameters at A = 47.1056, x_0 = 2.7659, b = 0.0003, and L = 0.9968 give the R^2 = 0.9894.

$$k(d\text{-OO}|T) = L/(1 + \exp(A \times (d\text{-OO} - x_0))) + b \quad (2)$$

Then the total performance of J-PtNW is calculated by mapping the sample statistic to total 12 400 pairs

$$p_{NW}(T) = \left(\sum_{i=0}^{N_s} k(d\text{-OO}_i|T)\right) \times \left(\frac{N_t - N_h}{N_S}\right) \quad (3)$$

where N_t is the total number of bridge pairs, N_h is the high coordination bridge pairs, and N_S is the sampled bridge pairs (here, N_t = 21 057, N_h = 8657, and N_S = 500) and $k(d\text{-OO}/T)$ is the fitted sigmoid function at temperature T.

The experiments showed that the J-PtNW performance is 50 times better than that of Pt/C at room temperature at mass activity. We considered that Pt/C is Pt (111) with 6926 surface Pt atoms, since the J-PtNW has 6926 Pt atoms in total with 3881 on the surface. In this way, we ensure the performance we are comparing is mass activity. This leads to 41 574 pairs. Therefore, the performance of Pt (111) can be estimated as follows

$$p_{pt(111)}(T) = k(d\text{-OO}_0|T) \times N_0 \quad (4)$$

where N_0 = 41 574 is the total number of bridge pairs and $k(d\text{-OO}_0|T)$ is the reaction rate for Pt (111) at temperature T.

We then define an improvement of the performance as PI(T), which is dependent on temperature and calculated by formula 5

$$\mathrm{PI}(T) = p_{NW}(T)/p_{pt(111)}(T) \quad (5)$$

Figure 5 shows the temperature dependence of the estimated performance improvement. At room temperature, our model leads to PI = 212.21 for the J-PtNW. This is a factor of 4 higher than the experimental PI = 50.[29] We consider that this agreement validates our explanation. This model allows us to

https://dx.doi.org/10.1021/jacs.9b13218
J. Am. Chem. Soc. 2020, 142, 8625−8632

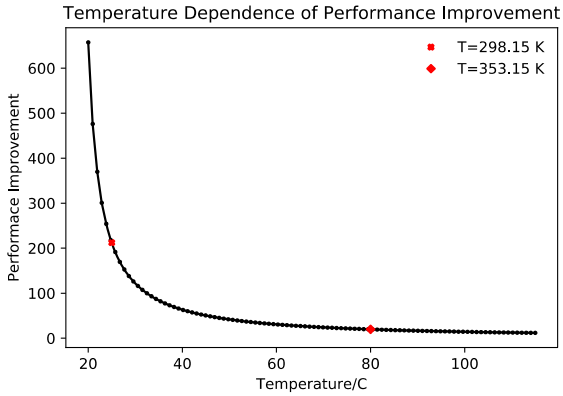

Figure 5. Temperature dependence of performance improvement, which is calculated by formula 4. With increasing temperature, the performance improvement decreases. PI at 298.15 K is marked in red; PI = 212.21 is 4 times larger than the experimental value, 50. Temperature limit of low-temperature PEMFCs is also marked as a red diamond; PI = 19.70 at 353.15 K.

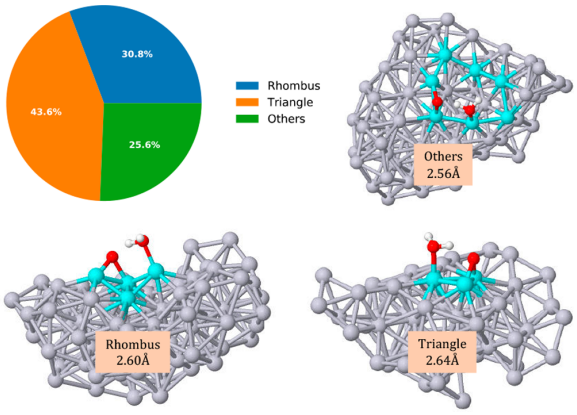

Figure 6. Identification results of barrierless sites (d-OO < 2.68 Å). Among the 72 barrierless sites, 30.8% of them are in the concave-up rhombus group and 43.6% of them are in the triangle group. One representative structure of each group is attached with their d-OO marked as well.

predict the performance improvement of J-PtNW at increased temperatures. For example, low-temperature PEMFCs use a water-based acidic polymer membrane as the electrolyte with platinum-based electrodes. Thus, the upper temperature limit is around 80 °C. Our model, estimates PI = 19.70 at 353.15 K (marked with a red diamond in Figure 5). Correcting by the same factor of 4, we predict the performance of J-PtNW should be around 5 times better than that of Pt (111) at 80 °C. This may provide guidance in choosing the optimal conditions for the real J-PtNW.

2.7. Active Sites Identification. To reveal the important features of the active sites and to provide insights for designing high-performance electrocatalysts, we characterized the structures of barrierless sites (d-OO ≤ 2.68 Å). They account for 72 out of the 500 bridge nanoclusters sampled. Among these 72 structures, many share similar geometric features. Thus, we further partitioned them into three subgroups: (I1) concave-up rhombus (30.8%); (I2) triangle (43.6%); (I3) others (25.6%).

Figure 6 shows one representative structure from each group. We consider that the triangle group and concave-up rhombus group play an important role in the dramatically improved performance. We summarized their geometry features and analyzed their statistics among the 500 structures in the following session.

2.7.1. Triangle Group Statistics. As shown in Figure 6, triangle group I2 is an important part of the barrierless sites (43.6%). We define a structure as a triangle structure if its three Pts, the one binding water and the other two binding O, form a closed ring, marked in cyan in Figure 6. On the basis of this definition, we picked out all triangle structures from the 500 sampled bridge nanoclusters and plotted their distribution toward d-OO in Figure 7. There are 143 triangles in the sample with the main peak located at ~2.75 Å. Although several triangles showed a large d-OO (one representative structure of a bad triangle is shown in Figure 7), we see that a major percentage of the triangles led to dramatically improved performance of the J-PtNW. Thus, a synthetic strategy might focus on generating triangle structures. Additional triangle structures with various d-OO are shown in Figure S11 in the Supporting Information.

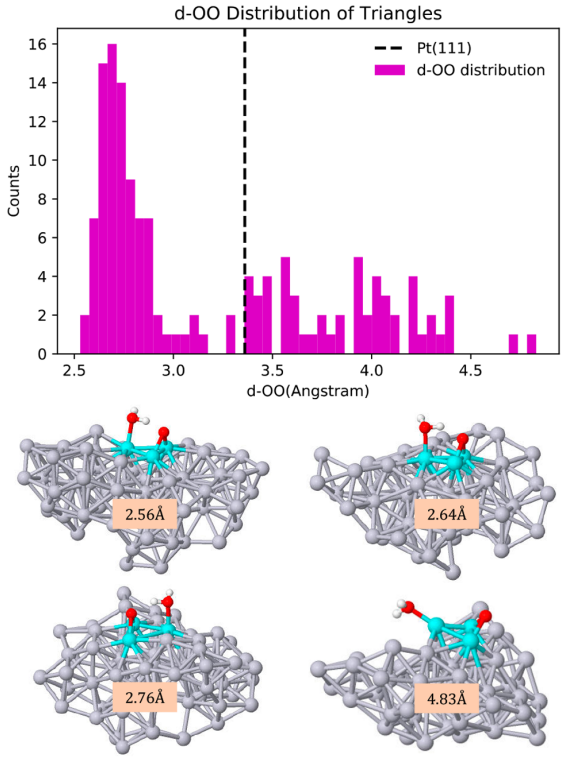

Figure 7. Statistics of the triangle group among 143 out of 500 sampled bridge nanoclusters. (Top) There are 143 triangles in total, and 87 of them show shorter d-OO than Pt (111). Small fraction of the triangles showed large d-OO, but main peak is located way left from Pt (111) (dashed line in the plot). (Bottom) Four representative structures of different d-OO. More structures are included in Figure S11 in the Supporting Information.

2.7.2. Concave-Up Rhombus Group Statistics. We then examined all concave-up rhombus structures among the 500 sampled bridge nanoclusters. The concave-up rhombus is

https://dx.doi.org/10.1021/jacs.9b13218
J. Am. Chem. Soc. 2020, 142, 8625−8632

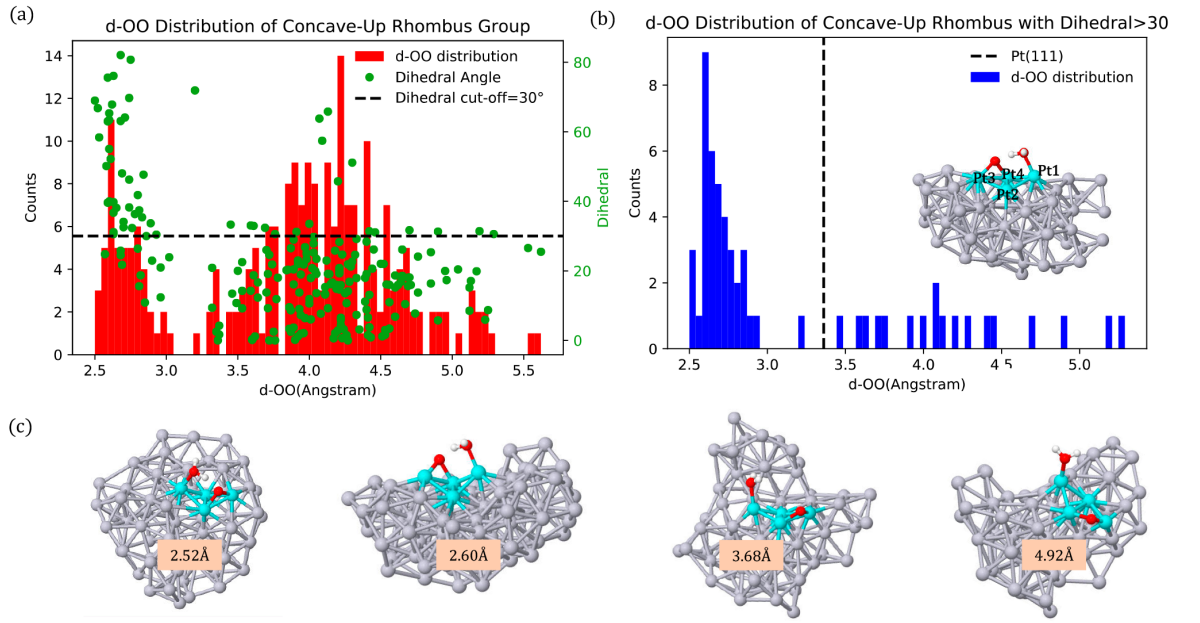

Figure 8. Statistics of the concave-up rhombus among 234 out of 500 sampled bridge nanoclusters. (a) Correlation between the dihedral angle and *d*-OO is shown. Here, the dihedral angle is defined as the angle between two surfaces defined by (Pt1, Pt2, Pt4) and (Pt2, Pt3, Pt4). As we could see, the rhombus with a dihedral angle larger than 30° mostly shows short *d*-OO. (b) Statistics of the concave-up rhombus with dihedral angle > 30°. Most of structures in this group shows a small *d*-OO with the main peak located at 2.6 Å. (c) Four representative structures with different *d*-OO are attached here, and more structures are available in Figure S12 in the Supporting Information.

defined as follows: three Pts, one Pt binding H_2O, and the other two Pts binding O, which cannot form a closed ring. Instead, another surface Pt is required to close the ring, forming a concave-up rhombus. As shown in Figure 8, we then define the dihedral angle of a rhombus as the dihedral angle between two surfaces defined by (Pt1, Pt2, Pt4) and (Pt2, Pt3, Pt4). The larger dihedral angle is, the more concave-up the rhombus is. There are a total number of 234 rhombi out of 500 with different dihedral angles We plotted the correlation between the dihedral angle and *d*-OO in Figure 8a, and we found the concave-up rhombus with a dihedral angle larger than 30° mostly shows short *d*-OO.

Thus, if we cut off the dihedral angle to 30°, the population of the active concave-up rhombic becomes 57 out of 500. Therefore, we define our active concave-up rhombic as those with dihedral angle > 30°. These 57 active concave-up rhombi are plotted in Figure 8b, along with several representative structures shown in Figure 8c. More structures with different *d*-OO distances are available in Figure S12 in the Supporting Information

2.8. Comparison with Previous Literature. The above discussion shows the atomistic explanation of the dramatically improved the performance. Thus, the jagged NW has many sites with a concave nature that push the OH bond of the H_2O_{ads} toward O_{ads}, leading to a dramatically reduced energy barrier for O_{ads} hydration. Earlier, Huang and co-workers suggested that mechanical strain, high ECSA, and under-coordinated surface Pt atoms may affect this remarkably accelerated ORR activity.[29] Consistent with the previous literature results, our analysis also finds numerous under-coordinated Pt surface atoms and a high 56.0% surface atom ratio (section 2.1), which will affect the ECSA.

To correlate the mechanical strain with catalytic activity, we plotted E_a versus the strain of the selected 18 structures from section 2.5. Here, we used the average Pt−Pt bond length around the adsorption sites to represent the local strain. As shown in Figure S13 of the Supporting Information, there is a linear correlation between the catalytic activity and the strain. In general, the sites with compressive strains show lower energy barriers, and sites with tensile strains show higher energy barriers. The correlation is weak with small R^2 at 0.46, but we agree that mechanical strain plays a role in the reduced energy barrier of O_{ads} hydration. Our work, with overall agreement with experiment in NW structure characterization and performance prediction, explains the dramatically improved ORR of J-PtNW from a very different atomistic perspective.

3. CONCLUSION

Starting from the J-PtNW synthesized using the ReaxFF reactive force field, we developed the bridge nanocluster model for DFT calculations. Using sites randomly selected from the surface, we observed a strong correlation between *d*-OO and the free energy barrier G_a of the RDS, O_{ads} hydration. This dramatically reduced the computational cost but accurately described the performance of each bridge pair. We found 14.4% of the sampled surface sites are barrierless for the RDS. Identification of these active sites led to two groups sharing similar geometrical patterns, the triangle group and the concave-up rhombus. Using the model developed above, we could predict the performance improvement of the whole J-PtNW. We report the atomistic structure of the active sites, which provides some insights in designing high-performance electrocatalysts for ORR.

https://dx.doi.org/10.1021/jacs.9b13218
J. Am. Chem. Soc. 2020, 142, 8625−8632

■ ASSOCIATED CONTENT

Supporting Information

The Supporting Information is available free of charge at https://pubs.acs.org/doi/10.1021/jacs.9b13218.

Description of DFT calculations, transition state search used in this work, benchmark calculations for bridge nanocluster model, more structures of triangle and concave-up rhombic groups, and additional calculations (PDF)

■ AUTHOR INFORMATION

Corresponding Author

William A. Goddard III − *Materials and Process Simulation Center (MSC) and Joint Center for Artificial Photosynthesis (JCAP), California Institute of Technology, Pasadena, California 91125, United States;* orcid.org/0000-0003-0097-5716; Email: wag@caltech.edu

Authors

Yalu Chen − *Materials and Process Simulation Center (MSC) and Joint Center for Artificial Photosynthesis (JCAP), California Institute of Technology, Pasadena, California 91125, United States;* orcid.org/0000-0002-0589-845X

Tao Cheng − *Materials and Process Simulation Center (MSC) and Joint Center for Artificial Photosynthesis (JCAP), California Institute of Technology, Pasadena, California 91125, United States; Institute of Functional Nano & Soft Materials (FUNSOM), Jiangsu Key Laboratory for Carbon-Based Functional Materials & Devices, Joint International Research Laboratory of Carbon-Based Functional Materials and Devices, Soochow University, Suzhou, Jiangsu 215123, People's Republic of China;* orcid.org/0000-0003-4830-177X

Complete contact information is available at: https://pubs.acs.org/10.1021/jacs.9b13218

Notes

The authors declare no competing financial interest.

■ ACKNOWLEDGMENTS

This research was supported by ONR (N00014-18-1-2155). Y.C. was supported by the Joint Center for Artificial Photosynthesis, a DOE Energy Innovation Hub, supported through the Office of Science of the U.S. Department of Energy under Award Number DE-SC0004993. This work uses the Extreme Science and Engineering Discovery Environmen t(XSEDE), which is supported by National Science Foundation Grant Number ACI-1053575, and the computational resources of Caltech High Performance Computing Center (HPC).

■ REFERENCES

(1) Peighambardoust, S. J.; Rowshanzamir, S.; Amjadi, M. Review of the Proton Exchange Membranes for Fuel Cell Applications. *Int. J. Hydrogen Energy* **2010**, *35* (17), 9349−9384.

(2) Steele, B. C. H.; Heinzel, A. Materials for Fuel-Cell Technologies. *Nature* **2001**, *414* (6861), 345−352.

(3) Wang, S.; Jiang, S. P. Prospects of Fuel Cell Technologies. *Natl. Sci. Rev.* **2017**, *4* (2), 163−166.

(4) Shao, M.; Chang, Q.; Dodelet, J.-P.; Chenitz, R. Recent Advances in Electrocatalysts for Oxygen Reduction Reaction. *Chem. Rev.* **2016**, *116* (6), 3594−3657.

(5) Sui, S.; Wang, X.; Zhou, X.; Su, Y.; Riffat, S.; Liu, C. A Comprehensive Review of Pt Electrocatalysts for the Oxygen Reduction Reaction: Nanostructure, Activity, Mechanism and Carbon Support in PEM Fuel Cells. *J. Mater. Chem. A* **2017**, *5* (5), 1808−1825.

(6) He, Q.; Cairns, E. J. Review—Recent Progress in Electrocatalysts for Oxygen Reduction Suitable for Alkaline Anion Exchange Membrane Fuel Cells. *J. Electrochem. Soc.* **2015**, *162* (14), F1504−F1539.

(7) Huang, X.; Zhao, Z.; Chen, Y.; Zhu, E.; Li, M.; Duan, X.; Huang, Y. A Rational Design of Carbon-Supported Dispersive Pt-Based Octahedra as Efficient Oxygen Reduction Reaction Catalysts. *Energy Environ. Sci.* **2014**, *7* (9), 2957−2962.

(8) Peng, Z.; Yang, H. Designer Platinum Nanoparticles: Control of Shape, Composition in Alloy, Nanostructure and Electrocatalytic Property. *Nano Today* **2009**, *4* (2), 143−164.

(9) Wu, J.; Yang, H. Platinum-Based Oxygen Reduction Electrocatalysts. *Acc. Chem. Res.* **2013**, *46* (8), 1848−1857.

(10) Porter, N. S.; Wu, H.; Quan, Z.; Fang, J. Shape-Control and Electrocatalytic Activity-Enhancement of Pt-Based Bimetallic Nanocrystals. *Acc. Chem. Res.* **2013**, *46* (8), 1867−1877.

(11) Wang, D.; Xin, H. L.; Hovden, R.; Wang, H.; Yu, Y.; Muller, D. A.; DiSalvo, F. J.; Abruña, H. D. Structurally Ordered Intermetallic Platinum-Cobalt Core-Shell Nanoparticles with Enhanced Activity and Stability as Oxygen Reduction Electrocatalysts. *Nat. Mater.* **2013**, *12* (1), 81−87.

(12) Mazumder, V.; Chi, M.; More, K. L.; Sun, S. Core/Shell Pd/FePt Nanoparticles as an Active and Durable Catalyst for the Oxygen Reduction Reaction. *J. Am. Chem. Soc.* **2010**, *132* (23), 7848−7849.

(13) Stamenkovic, V. R.; Fowler, B.; Mun, B. S.; Wang, G.; Ross, P. N.; Lucas, C. A.; Marković, N. M. Improved Oxygen Reduction Activity on Pt3Ni(111) via Increased Surface Site Availability. *Science* **2007**, *315* (5811), 493−497.

(14) Choi, S.-I.; Xie, S.; Shao, M.; Odell, J. H.; Lu, N.; Peng, H.-C.; Protsailo, L.; Guerrero, S.; Park, J.; Xia, X.; Wang, J.; Kim, M. J.; Xia, Y. Synthesis and Characterization of 9 Nm Pt-Ni Octahedra with a Record High Activity of 3.3 A/MgPt for the Oxygen Reduction Reaction. *Nano Lett.* **2013**, *13* (7), 3420−3425.

(15) Huang, X.; Zhao, Z.; Cao, L.; Chen, Y.; Zhu, E.; Lin, Z.; Li, M.; Yan, A.; Zettl, A.; Wang, Y. M.; Duan, X.; Mueller, T.; Huang, Y. High-Performance Transition Metal-Doped Pt3Ni Octahedra for Oxygen Reduction Reaction. *Science* **2015**, *348* (6240), 1230−1234.

(16) Wang, Y.-J.; Zhao, N.; Fang, B.; Li, H.; Bi, X. T.; Wang, H. Carbon-Supported Pt-Based Alloy Electrocatalysts for the Oxygen Reduction Reaction in Polymer Electrolyte Membrane Fuel Cells: Particle Size, Shape, and Composition Manipulation and Their Impact to Activity. *Chem. Rev.* **2015**, *115* (9), 3433−3467.

(17) Lu, Y.; Thia, L.; Fisher, A.; Jung, C.-Y.; Yi, S. C.; Wang, X. Octahedral PtNi Nanoparticles with Controlled Surface Structure and Composition for Oxygen Reduction Reaction. *Sci. China Mater.* **2017**, *60* (11), 1109−1120.

(18) Hasché, F.; Oezaslan, M.; Strasser, P. Activity and Structure of Dealloyed PtNi3 Nanoparticle Electrocatalyst for Oxygen Reduction Reaction in PEMFC. *ECS Trans.* **2011**, *41* (1), 1079−1088.

(19) Mani, P.; Srivastava, R.; Strasser, P. Dealloyed Binary PtM3 (M = Cu, Co, Ni) and Ternary PtNi3M (M = Cu, Co, Fe, Cr) Electrocatalysts for the Oxygen Reduction Reaction: Performance in Polymer Electrolyte Membrane Fuel Cells. *J. Power Sources* **2011**, *196*, 666.

(20) Jia, Q.; Caldwell, K.; Strickland, K.; Ziegelbauer, J. M.; Liu, Z.; Yu, Z.; Ramaker, D. E.; Mukerjee, S. Improved Oxygen Reduction Activity and Durability of Dealloyed PtCox Catalysts for Proton Exchange Membrane Fuel Cells: Strain, Ligand, and Particle Size Effects. *ACS Catal.* **2015**, *5* (1), 176−186.

(21) Strasser, P.; Koh, S.; Yu, C. Voltammetric Surface Dealloying of Pt Bimetallic Nanoparticles: A Novel Synthetic Method Towards More Efficient ORR Electrocatalysts. *ECS Trans.* **2007**, *11* (1), 167−180.

(22) Strasser, P.; Koh, S.; Anniyev, T.; Greeley, J.; More, K.; Yu, C.; Liu, Z.; Kaya, S.; Nordlund, D.; Ogasawara, H.; Toney, M. F.;

Nilsson, A. Lattice-Strain Control of the Activity in Dealloyed Core-Shell Fuel Cell Catalysts. *Nat. Chem.* **2010**, *2* (6), 454−460.
(23) Debe, M. K. Electrocatalyst Approaches and Challenges for Automotive Fuel Cells. *Nature* **2012**, *486* (7401), 43−51.
(24) van der Vliet, D.; Wang, C.; Debe, M.; Atanasoski, R.; Markovic, N. M.; Stamenkovic, V. R. Platinum-Alloy Nanostructured Thin Film Catalysts for the Oxygen Reduction Reaction. *Electrochim. Acta* **2011**, *56* (24), 8695−8699.
(25) Debe, M. K.; Steinbach, A. J.; Vernstrom, G. D.; Hendricks, S. M.; Kurkowski, M. J.; Atanasoski, R. T.; Kadera, P.; Stevens, D. A.; Sanderson, R. J.; Marvel, E.; Dahn, J. R. Extraordinary Oxygen Reduction Activity of Pt3Ni7. *J. Electrochem. Soc.* **2011**, *158* (8), B910−B918.
(26) Stevens, D. A.; Mehrotra, R.; Sanderson, R. J.; Vernstrom, G. D.; Atanasoski, R. T.; Debe, M. K.; Dahn, J. R. Dissolution of Ni from High Ni Content Pt1-xNix Alloys. *J. Electrochem. Soc.* **2011**, *158* (8), B905−B909.
(27) van Duin, A. C. T.; Dasgupta, S.; Lorant, F.; Goddard, W. A. ReaxFF: A Reactive Force Field for Hydrocarbons. *J. Phys. Chem. A* **2001**, *105* (41), 9396−9409.
(28) Fortunelli, A.; Goddard, W. A., III; Sementa, L.; Barcaro, G.; Negreiros, F. R.; Jaramillo-Botero, A. The Atomistic Origin of the Extraordinary Oxygen Reduction Activity of Pt3Ni7 Fuel Cell Catalysts. *Chemical Science* **2015**, *6* (7), 3915−3925.
(29) Li, M.; Zhao, Z.; Cheng, T.; Fortunelli, A.; Chen, C.-Y.; Yu, R.; Zhang, Q.; Gu, L.; Merinov, B. V.; Lin, Z.; Zhu, E.; Yu, T.; Jia, Q.; Guo, J.; Zhang, L.; Goddard, W. A.; Huang, Y.; Duan, X. Ultrafine Jagged Platinum Nanowires Enable Ultrahigh Mass Activity for the Oxygen Reduction Reaction. *Science* **2016**, *354* (6318), 1414−1419.
(30) Cheng, T.; Goddard, W. A.; An, Q.; Xiao, H.; Merinov, B.; Morozov, S. Mechanism and Kinetics of the Electrocatalytic Reaction Responsible for the High Cost of Hydrogen Fuel Cells. *Phys. Chem. Chem. Phys.* **2017**, *19* (4), 2666−2673.
(31) Noël, J.-M.; Latus, A.; Lagrost, C.; Volanschi, E.; Hapiot, P. Evidence for OH Radical Production during Electrocatalysis of Oxygen Reduction on Pt Surfaces: Consequences and Application. *J. Am. Chem. Soc.* **2012**, *134* (5), 2835−2841.
(32) Anderson, A. B.; Albu, T. V. Catalytic Effect of Platinum on Oxygen Reduction An Ab Initio Model Including Electrode Potential Dependence. *J. Electrochem. Soc.* **2000**, *147* (11), 4229−4238.
(33) Sha, Y.; Yu, T. H.; Merinov, B. V.; Shirvanian, P.; Goddard, W. A. Oxygen Hydration Mechanism for the Oxygen Reduction Reaction at Pt and Pd Fuel Cell Catalysts. *J. Phys. Chem. Lett.* **2011**, *2* (6), 572−576.
(34) Sha, Y.; Yu, T. H.; Merinov, B. V.; Goddard, W. A. Prediction of the Dependence of the Fuel Cell Oxygen Reduction Reactions on Operating Voltage from DFT Calculations. *J. Phys. Chem. C* **2012**, *116* (10), 6166−6173.
(35) Huang, Y.; Chen, Y.; Cheng, T.; Wang, L.-W.; Goddard, W. A. Identification of the Selective Sites for Electrochemical Reduction of CO to C_{2+} Products on Copper Nanoparticles by Combining Reactive Force Fields, Density Functional Theory, and Machine Learning. *ACS Energy Letters* **2018**, *3*, 2983−2988.
(36) Cheng, T.; Xiao, H.; Goddard, W. A. Nature of the Active Sites for CO Reduction on Copper Nanoparticles; Suggestions for Optimizing Performance. *J. Am. Chem. Soc.* **2017**, *139* (34), 11642−11645.
(37) Chen, Y.; Huang, Y.; Cheng, T.; Goddard, W. A. Identifying Active Sites for CO2 Reduction on Dealloyed Gold Surfaces by Combining Machine Learning with Multiscale Simulations. *J. Am. Chem. Soc.* **2019**, *141* (29), 11651−11657.
(38) Cheng, T.; Huang, Y.; Xiao, H.; Goddard, W. A. Predicted Structures of the Active Sites Responsible for the Improved Reduction of Carbon Dioxide by Gold Nanoparticles. *J. Phys. Chem. Lett.* **2017**, *8* (14), 3317−3320.
(39) Kresse, G.; Hafner, J. Ab Initio Molecular-Dynamics Simulation of the Liquid-Metal–Amorphous-Semiconductor Transition in Germanium. *Phys. Rev. B: Condens. Matter Mater. Phys.* **1994**, *49* (20), 14251−14269.
(40) Henkelman, G.; Uberuaga, B. P.; Jónsson, H. A Climbing Image Nudged Elastic Band Method for Finding Saddle Points and Minimum Energy Paths. *J. Chem. Phys.* **2000**, *113* (22), 9901−9904.
(41) Mathew, K.; Sundararaman, R.; Letchworth-Weaver, K.; Arias, T. A.; Hennig, R. G. Implicit Solvation Model for Density-Functional Study of Nanocrystal Surfaces and Reaction Pathways. *J. Chem. Phys.* **2014**, *140* (8), 084106.

https://dx.doi.org/10.1021/jacs.9b13218
J. Am. Chem. Soc. 2020, 142, 8625−8632